IEEE Access
Multidisciplinary | Rapid Review | Open Access Journal

Received October 8, 2019, accepted October 16, 2019, date of publication October 21, 2019, date of current version October 30, 2019.

Digital Object Identifier 10.1109/ACCESS.2019.2948421

The Three Dimension First-Order Symplectic Partitioned Runge-Kutta Scheme Simulation for GPR Wave Propagation in Pavement Structure

MAN YANG[1,2,3], HONGYUAN FANG[1,2,3], FUMING WANG[1,2,3], HEYANG JIA[1,2,3], JIANWEI LEI[1,2,3], AND DI ZHANG[4]

[1]College of Water Conservancy and Environmental Engineering, Zhengzhou University, Zhengzhou 450001, China
[2]National Local Joint Engineering Laboratory of Major Infrastructure Testing And Rehabilitation Technology, Zhengzhou 450001, China
[3]Collaborative Innovation Center of Water Conservancy and Transportation Infrastructure Safety, Zhengzhou 450001, China
[4]Yellow River Conservancy Technical Institute, Kaifeng 475000, China

Corresponding author: Hongyuan Fang (18337192244@163.com)

This work was supported in part by the National Key Research and Development Program of China under Grant 2017YFC1501200, in part by the National Natural Science Foundation of China under Grant 51678536 and Grant 51978630, in part by the Program for Science and Technology Innovation Talents in Universities of Henan Province under Grant 19HASTIT043, in part by the Outstanding Young Talent Research Fund of Zhengzhou University under Grant 1621323001, and in part by the Program for Innovative Research Team (Science and Technology), University of Henan Province, under Grant 18IRTSTHN007.

ABSTRACT Numerical simulation of three-layer layered electromagnetic waves is key problem for nondestructive testing of ground penetrating radar (GPR) pavement. In this paper, the difference iterative scheme of three-dimensional first-order symplectic partitioned Rung-Kutta is derived, which is applied to pavement detection of ground penetrating radar by using Higdon ABC boundary condition. Incident waves are considered as line sources. The accuracy and efficiency of the proposed algorithm are verified by the traditional 3D-FDTD algorithm. The results indicate that the accuracy and efficiency between the two methods are consistent. Unlike the traditional 3D-FDTD algorithm, the CPU time of the proposed method is reduced by 30%. The diseases location of the pavement structure is directly reflected by the numerical simulation result of the proposed method. This provides a three-dimensional symplectic partitioned Rung-Kutta algorithm, which can be applied to the forward simulation of GPR. It provides a three-dimensional symplectic partitioned Rung-Kutta algorithm, which can be applied to the forward simulation of GPR. The accurate electromagnetic response information of the target can be obtained by the proposed method.

INDEX TERMS Ground penetrating radar (GPR), symplectic partitioned runge-kutta method, pavement structure, higdon ABC.

I. INTRODUCTION

In the last decades, ground penetrating radar (GPR) inspection research which was carried in road section of structural damage has obtained considerable attention [1]. GPR is a nondestructive testing tool, which can quickly demonstrate the location of road surface underground diseases [2], [3]. The image detected by GPR can clearly show the thickness of the pavement, the buried depth of abnormal body and so on. Three-dimensional forward simulation of GPR is helpful to interpret the measured signal of GPR [4]–[6].

The associate editor coordinating the review of this manuscript and approving it for publication was Giorgio Montisci.

There are many different methods for three-dimensional numerical simulation of GPR [7]. Huang *et al.* [8] have proposed a new ray-tracing method in 3-D heterogeneous isotropic media based on the bilinear travel-time interpolation and wavefront group marching method (GMM). Schmidt and Lee [9] have implemented and analyzed the Rokhlin-Greengard fast multipole method for evaluating coulomb and multipole potentials in three dimensions. Negri *et al.* [10] have carried out ground-penetrating radar (GPR) survey in an area located near the archaeological excavations. Dai *et al.* [11] have eliminated the super strong reflection on the interceptive boundary by the

finite element method (FEM) numerical simulation for GPR. Namiki [12] has previously introduced the alternating direction implicit finite-difference time domain (ADI-FDTD) method. Li *et al.* [13] have derived the 3D high-order finite-difference time domain (FDTD) method with CFS-RIPML boundary and applied it in GPR forward simulation. Although these algorithms have made some achievements, there are still some shortcomings in accuracy and efficiency of GPR forward simulation. For instance, the ray-tracing method is used to simulate the complicated structure difficultly, the computational efficiency of FDTD method is limited by the stability of CFL condition [14] and the ADI-FDTD [15] is restricted by the numerical error or the accuracy requirement.

At present, FDTD method is commonly used in three-dimension forward modeling of GPR, however, it costs great amount of CPU time to calculate the model by using the 3D-FDTD method [16], [17]. Due to the iterative formula of SPRK algorithm is less than that of FDTD method, the computational efficiency of SPRK algorithm is studied and applied by researchers. Gladwell *et al.* [18] have shown the Hamiltonian of a class of symplectic partitioned Rung-Kutta (SPRK) scheme. Tang *et al.* [19] have presented a more effective method to construct high-order symplectic integrators for solving second order Hamiltonian equations. Kuang *et al.* [20] have proposed a new high-order symplectic compact finite-difference time-domain (FDTD) method in order to reduce the numerical dispersion error. He and Li [21] have obtained a sufficient and necessary condition for the existence of symplectic critical surfaces in two-dimensional complex space forms. Huang and Wu [22] have constructed a symplectic partitioned Rung-Kutta (SPRK) scheme for approximating the solution to infinite dimensional non-separable Hamiltonian systems of Maxwell's equations for the first time. Fang *et al.* [23] have proposed the SPRK method for applying GPR to road quality detection in two-dimension forward simulation. Although the SPRK algorithm has been applied in pavement structure, however, its application of GPR is applied in two-dimensional space and the profile of GPR can not intuitively reflect the specific distribution of media in three-dimensional pavement structure.

In this paper, Hamiltonian system and SPRK method is introduced, and three-dimensional governing equations are proposed for the first time. The absorbing boundary condition is second-order Higdon ABC boundary. Two three-dimensional pavement structure models are applied to the GPR detection by the SPRK method.

II. HAMILTONIAN SYSTEM AND SPRK METHOD

The following general Hamiltonian system of canonical equations can be written as [24], [25]

$$\begin{cases} \dfrac{dp}{dt} = -\dfrac{\partial H}{\partial q} = f(q,p), \\ \dfrac{dq}{dt} = \dfrac{\partial H}{\partial p} = g(q,p). \end{cases} \tag{1}$$

where $H(q,p)$ is the Hamiltonian functions. Let us suppose that the component q of the first set of system (1) are integrated by an R-K method and the component q in second part of system are integrated with a different R-K method. The overall scheme is called a Partitioned Roung-Kutta method, or shortly called P-R-K method. A s-stage partitioned Runge-Kutta method can be applied with Butecher tableau

$$\begin{array}{c|ccc} c_1 & a_{11} & \cdots & a_{1s} \\ \vdots & \vdots & & \vdots \\ c_s & a_{s1} & \cdots & a_{ss} \\ \hline & b_1 & \cdots & b_s \end{array} \qquad \begin{array}{c|ccc} C_1 & A_{11} & \cdots & A_{1s} \\ \vdots & \vdots & & \vdots \\ C_s & A_{s1} & \cdots & A_{ss} \\ \hline & B_1 & \cdots & B_s \end{array} \tag{2}$$

The Eq. (1) may have the following relation

$$\begin{cases} P_i = p^n + \beta \sum_{j=1}^{s} a_{ij} f(P_j, Q_j), \\ Q_i = q^n + \beta \sum_{j=1}^{s} A_{ij} g(P_j, Q_j), \\ p^{n+1} = p^n + \beta \sum_{i=1}^{s} b_i f(P_i, Q_i), \\ q^{n+1} = q^n + \beta \sum_{i=1}^{s} B_i f(P_i, Q_i), \end{cases} \quad i = 1, 2, \cdots, s \tag{3}$$

where β denotes time increment. P_j and Q_j are j-stage partitioned polynomial. These tableaux are coefficients of P-R-K method.

If the parameter of Eq. (2) satisfies the relationship as follows

$$\begin{aligned} b_i A_{ij} + B_i a_{ji} - b_i B_j &= 0 \\ b_i = B_i, \quad i, j &= 1, \ldots, s \end{aligned} \tag{4}$$

then the s-stage PRK method is considered as sympletic.

The coefficients of first-order symplectic PRK method can be expressed as

$$\begin{array}{c|c} 0 & 1 \\ \hline & 1 \end{array} \qquad \begin{array}{c|c} 0 & 0 \\ \hline & 1 \end{array} \tag{5}$$

III. GOVERNING EQUATIONS

Maxwell's equations can be written as

$$\begin{cases} \nabla \times \mathbf{E} = -\dfrac{\partial \mathbf{B}}{\partial t} = -\mu \dfrac{\partial \mathbf{H}}{\partial t} \\ \nabla \times \mathbf{H} = \dfrac{\partial \mathbf{D}}{\partial t} + \mathbf{J} = \varepsilon \dfrac{\partial \mathbf{E}}{\partial t} + \sigma \mathbf{E} \end{cases} \tag{6}$$

where, **D**, **B**, **J**, **E** and **H** denote electric flux density, magnetic flux density, current density, electric field vector and magnetic field vector, respectively. The electric flux density $\mathbf{D} = \varepsilon \mathbf{E}$, the magnetic flux density $\mathbf{B} = \mu \mathbf{H}$, the current density $\mathbf{J} = \sigma \mathbf{E}$, where ε, μ, and σ are expressed as permittivity, permeability, and conductivity, respectively.

By letting $\mathbf{H} = \nabla \times \mathbf{A}$ and $\mathbf{E} = -\mathbf{U}$, the generalized Hamiltonian function in lossy media is given by

$$H(\mathbf{A}, \mathbf{U}) = \int \left(\frac{1}{2\mu} |\mathbf{U}|^2 + \frac{1}{2\varepsilon} |\nabla \times \mathbf{A}|^2 - \frac{1}{\varepsilon} \mathbf{J}\mathbf{A} \right) dV \tag{7}$$

Inserting Eq. (7) into Eq. (8), the equation of the electromagnetic field can be expressed as

$$\begin{cases} \dfrac{\partial \mathbf{A}}{\partial t} = \dfrac{d\mathbf{H}}{d\mathbf{U}} = \dfrac{1}{\mu}\mathbf{U} \\ \dfrac{\partial \mathbf{U}}{\partial t} = -\dfrac{d\mathbf{H}}{d\mathbf{A}} = \dfrac{1}{\varepsilon}\nabla^2\mathbf{A} - \dfrac{\sigma}{\varepsilon}\mathbf{U} \end{cases} \tag{8}$$

It is well known that the electric field and the magnetic field differ by halftime step intervals in three-dimensional Yee cell, however the difference method of the three-dimensional first-order symplectic algorithm is different. The node value of **U** and **A** is defined at the same spatial grid point and at the same time step. When applied in Eq. (5) with Eq. (8), the first order 3-D SPRK method can be written as

$$\begin{cases} U^1_{i,j,k} = U^n_{i,j,k} \\ A^1_{i,j,k} = A^n_{i,j,k} + \dfrac{\Delta t}{\mu} U^1_{i,j,k} \\ U^{n+1}_{i,j,k} = U^n_{i,j,k} + \Delta t \left(\dfrac{1}{\varepsilon}\nabla^2 A^1_{i,j,k} - \dfrac{\sigma}{\varepsilon} U^1_{i,j,k} \right) \\ A^{n+1}_{i,j,k} = A^n_{i,j,k} + \dfrac{\Delta t}{\mu} U^1_{i,j,k} \end{cases} \tag{9}$$

The Eq. (9) is simplified to obtain the formula of the first-order SPRK method as follows

$$\begin{cases} U^{n+1}_{i,j,k} = \dfrac{\varepsilon - \Delta t\sigma}{\varepsilon} U^n_{i,j,k} + \dfrac{\Delta t}{\varepsilon}\nabla^2 A^{n+1}_{i,j,k} \\ A^{n+1}_{i,j,k} = A^n_{i,j,k} + \dfrac{\Delta t}{\mu} U^n_{i,j,k} \end{cases} \tag{10}$$

where $A^n_{i,j,k}$ and $U^n_{i,j,k}$ denote the nodal values of **A** and **U** at the space point (i, j, k) and n-th time step, respectively. Using central difference to approximate the 3-D Laplacian operator and letting $\Delta x = \Delta y = \Delta z = \delta$ yield

$$\begin{aligned} \nabla^2 A^n_{i,j,k} = {} & \frac{A^n_{i-1,j,k} + A^n_{i+1,j,k} + A^n_{i,j-1,k} + A^n_{i,j+1,k}}{\delta^2} \\ & + \frac{A^n_{i,j,k+1} + A^n_{i,j,k-1} - 6A^n_{i,j,k}}{\delta^2} \end{aligned} \tag{11}$$

IV. ABSORBING BOUNDARY CONDITION

The N-order absorption boundary condition have been proposed by Higdon [26], [27] can be expressed as

$$\left(\prod_{j=1}^{N} (\cos\alpha_j \frac{\partial}{\partial t} - c\frac{\partial}{\partial x}) \right) U = 0 \tag{12}$$

where α_j denotes incoming angle of absorption, c denotes wave speed. Then reflection coefficient of Eq. (12) is expressed as

$$-\prod_{j=1}^{N} \left(\frac{\cos\alpha_j - \cos\theta}{\cos\alpha_j + \cos\theta} \right) \tag{13}$$

where θ is the entry angle, the condition operator of the absorption boundary can be expressed as

$$B = \prod_{j=1}^{N} \left(\beta_j \frac{\partial}{\partial t} - v_p \frac{\partial}{\partial x} \right) \tag{14}$$

where N is the order used to absorb the boundary condition and β_j is a positive integer.

In this paper, the second-order Higdon ABC absorption boundary condition is used

$$\left(\prod_{j=1}^{2} (\cos\alpha_j \frac{\partial}{\partial t} - c\frac{\partial}{\partial x}) \right) U = 0 \tag{15}$$

where c is velocity of light and $|\alpha_j| \le \pi/2$ for all j.

The offset operator for space x-, y-, z- direction and time t can be defined as

$$\begin{cases} U_x \cdot U^n_{i,j,k} = U^n_{i+1,j,k} \\ U_y \cdot U^n_{i,j,k} = U^n_{i,j+1,k} \\ U_z \cdot U^n_{i,j,k} = U^n_{i,j,k+1} \\ U_t \cdot U^n_{i,j,k} = U^{n+1}_{i,j,k} \end{cases} \tag{16}$$

To derive finite difference formulation, the time and space differential operators are discrete as

$$\begin{aligned} \frac{\partial}{\partial t} U^n_{i,j,k} &= \left(\frac{I - U_t^{-1}}{\Delta t} \right) U^n_{i,j,k} = \frac{U^n_{i,j,k} - U^{n-1}_{i,j,k}}{\Delta t} \\ \frac{\partial}{\partial x} U^n_{i,j,k} &= \left(\frac{I - U_t^{-1}}{\Delta x} \right) U_t^{-1} U^n_{i,j,k} \\ &= \left(\frac{U_x - I}{\Delta x} \right) U^{n-1}_{i,j,k} = \frac{U^{n-1}_{i+1,j,k} - U^{n-1}_{i,j,k}}{\Delta x} \end{aligned} \tag{17}$$

Therefore, the operator $\cos\alpha_j(\partial/\partial t) - c(\partial/\partial x)$ can be expressed as

$$\begin{aligned} B\left(U_x, U_t^{-1}\right) = {} & \beta_j \left(\frac{1 - U_t^{-1}}{\Delta t}\right)[(1-b)I + bU_x] \\ & - c\left(\frac{U_x - I}{\Delta x}\right)[(1-b)I + bU_t^{-1}] \end{aligned} \tag{18}$$

where I and b denote the identity operator and a weighting factor, respectively. And $\beta_j = \cos\alpha_j$. Therefore, the differential format of the absorption boundary acting on the wave field can be approximated as

$$\left[\prod_{j=1}^{2} B_j(U_x, U_t^{-1}) \right] U^n_{i,j,k} = 0 \tag{19}$$

To apply Eq. (19), simultaneous Eq. (18) and Eq. (19), the discrete form of boundary condition can be obtained as

$$\begin{aligned} U^n_{i,j,k} = {} & -\frac{1}{\eta_9}(\eta_1 U^{n-2}_{i+2,j,k} + \eta_2 U^{n-2}_{i+1,j,k} + \eta_3 U^{n-2}_{i,j,k} + \eta_4 U^{n-1}_{i+2,j,k} \\ & + \eta_5 U^{n-1}_{i+1,j,k} + \eta_6 U^n_{i,j,k} + \eta_7 U^n_{i+2,j,k} + \eta_8 U^n_{i+1,j,k}) \end{aligned} \tag{20}$$

where:

$$\begin{aligned} &\eta_1 = v_1^1 v_2^1 \quad \eta_2 = v_1^1 v_2^2 + v_1^2 v_2^1 \quad \eta_3 = v_1^2 v_2^2 \\ &\eta_4 = v_1^1 v_2^3 + v_1^3 v_2^1 \quad \eta_5 = v_1^1 v_2^4 + v_1^2 v_2^3 + v_1^3 v_2^2 + v_1^4 v_2^1 \\ &\eta_6 = v_1^2 v_2^4 + v_1^4 v_2^2 \quad \eta_7 = v_1^3 v_2^3 \quad \eta_8 = v_1^3 v_2^4 + v_1^4 v_2^3 \\ &\eta_9 = v_1^4 v_2^4 v_j^1 = -(p_j b + b) \end{aligned}$$

$$v_j^1 = -(p_j b + b) \quad v_j^2 = p_j b + b - 1 \quad v_j^3 = b - p_j(1-b)$$
$$v_j^4 = (1-a) - p_j(1-b) \quad p_j = c\Delta t/\beta_j \Delta x$$

In this paper, b, α_1 and α_2 are chosen as 1, 7.6° and 18.7°, respectively.

V. NUMERICAL EXAMPLES

First of all, a three-layered pavement model is established to verify the accuracy and efficiency of the proposed method. As shown in Fig. 1, the length, the width and the depth of the model is 80 cm, respectively. The first layer has a surface thickness of 20 cm, representative of asphalt concrete, has relative dielectric constant ε of 6, and the conductivity σ of 0.001 S/m. The second layer has a thickness of 20 cm, representative of cement stabilized macadam, has relative dielectric constant ε of 16, and the conductivity σ of 0.002 S/m. The third layer has a thickness of 40 cm, and has relative dielectric constant ε of 35 and the conductivity σ of 0.003 S/m. All materials are assumed to be non-magnetic $\mu = 1$. A Ricker pulse (Fig. 2) of unity amplitude and central frequency of 1GHz is used for excitation in 1-D symplectic PRK method. The position of the transmitting antenna is (0.4 m, 0.4 m, 0), and the position of the receiving antenna is (0.4 m, 0.48 m, 0). The time interval and the space increment are chosen 0.001 ns and 0.005 m, respectively. The computer processor is Inter (R) Core (TM) i7-8700K CPU @ 3.7 GHz. We used the Matlab R 2014a software for numerical simulation.

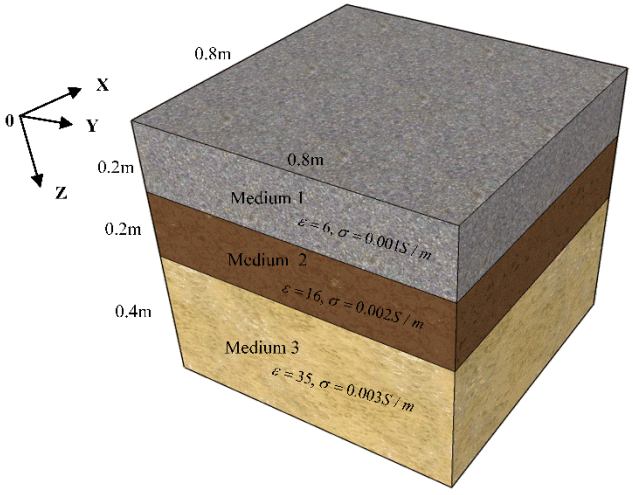

FIGURE 1. 3-D computational domain of the three-layered model.

The absolute error can be expressed as

$$absolute\ error = U - U_{ref} \tag{21}$$

The relative error is shown as

$$relative\ error = \left| \frac{U - U_{ref}}{U_{ref}} \right| \times 100\% \tag{22}$$

where U_{ref} is the reference solution calculated from the FDTD method over the whole time interval, U is the result

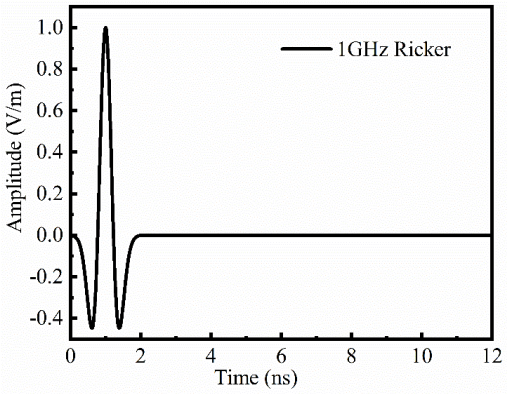

FIGURE 2. Ricker waveform of 1GHz central frequency fed into grid.

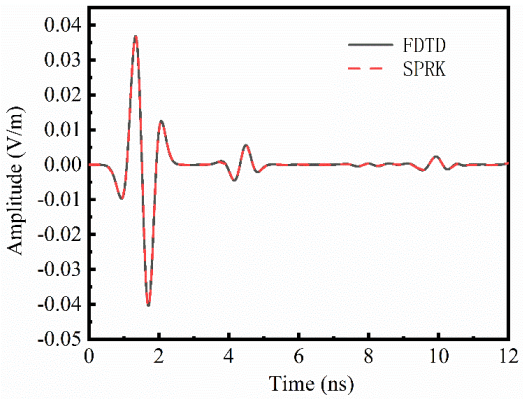

FIGURE 3. The numerical results calculated by the first order SPRK method (red dash line) and the FDTD method (black solid line).

from the SPRK scheme. As shown in Fig. 3, the numerical results calculated by the first order SPRK method (red dash line) and the FDTD method (black solid line) at the same time step. Excellent agreement is reached. Fig. 4 gives the absolute error of the amplitude of the electric field component computed by the FDTD method and the SPRK method. Fig. 5 shows the relative error of the amplitude of the **U** field component computed by the FDTD method and the SPRK method.

As can be seen from Fig. 4 and Fig. 5, the maximum absolute difference between the two methods is no more than 0.000001 V/m, and the relative difference between the two method is no more than 16%.

Table. 1 shows the CPU time cost and memory-consuming for SPRK method and FDTD method at the different time steps. The CPU time cost of SPRK method equals 2.231 h while the CPU time cost of the standard FDTD method equals 3.428h at time steps 3000. The CPU time cost of SPRK method equals 4.842 h while the CPU time cost of the standard FDTD method equals 6.211 h at time steps 6000. The CPU time cost of SPRK method equals 7.441 h while the CPU time cost of the standard FDTD method equals 10.161 h at time steps 12000. The memory consumed of SPRK method equals 1229.4 MB while the memory

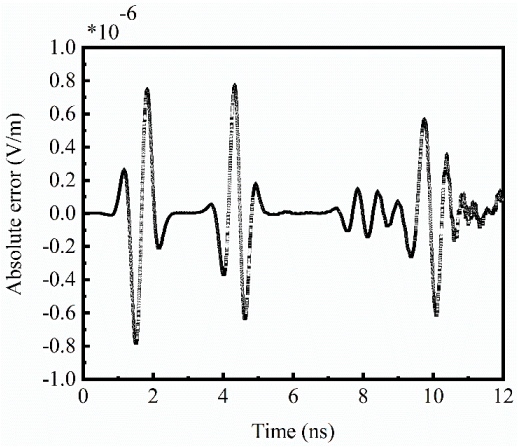

FIGURE 4. Absolute error of the amplitude of the electic field component computed by the FDTD method and the SPRK method.

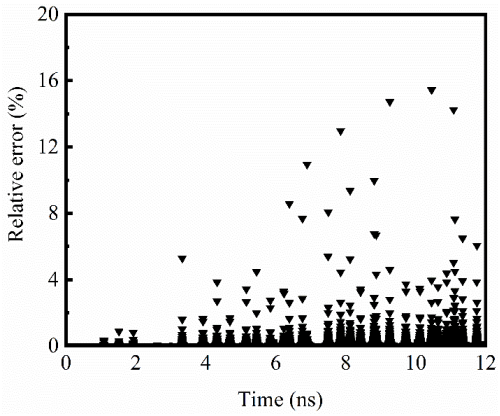

FIGURE 5. Relative error of the amplitude of the electric field component computed by the FDTD method and the SPRK method.

TABLE 1. CPU time and memeory consuming at the different time steps.

Method	Time steps	Time interval	CPU time	Memory consumed
SPRK	3000	0.001ns	2.231h	1229.4MB
SPRK	6000	0.001ns	4.842h	1389.1MB
SPRK	12000	0.001ns	7.441h	1429.4MB
FDTD	3000	0.001ns	3.428h	1221.8MB
FDTD	6000	0.001ns	6.211h	1296.4MB
FDTD	12000	0.001ns	10.161h	1327.3MB

consumed of the standard FDTD method equals 1221.8 MB at time steps 3000. The memory consumed of SPRK method equals 1389.1 MB while the memory consumed of the standard FDTD method equals 1296.4 MB at time steps 6000. The memory consumed of SPRK method equals 1429.4 MB while the memory consumed of the standard FDTD method equals 1327.3 MB at time steps 12000.

Based on comparisons, it may be concluded that the proposed method achieves almost the same level of accuracy as the standard FDTD method. The 3-D first-order SPRK algorithm consumes less CPU time than the standard FDTD scheme. The proposed method can save about 30% of the CPU time at the same time steps comparing with the FDTD method, but memory consumption only increases by less than 100 MB at same time steps.

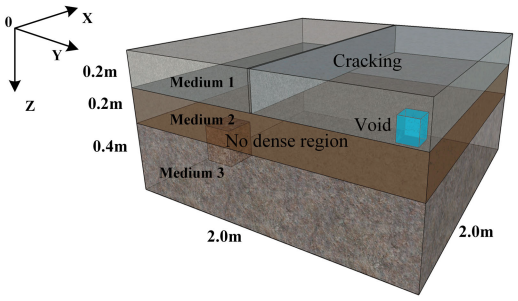

FIGURE 6. The structural diagram of complicated geoelectric model.

As a second example, the GPR profile of pavement section with structural damages is simulated (Fig. 6). The first layer has a surface thickness of 20 cm, representative of asphalt concrete, has relative dielectric constant ε of 6, and the conductivity σ of 0.001 S/m. There is a penetration crack in the middle of the first layer, and the width of the crack is 1 cm. The second layer has a thickness of 20 cm, representative of cement stabilized macadam, has relative dielectric constant ε of 16, and the conductivity σ of 0.002 S/m. In the second layer, there is a square void with length, width and height of 10cm. The relative dielectric constant ε of the void is 1, the conductivity σ is 0, and the center point of the void is set at (1.6 m, 1.6 m, 0.255 m). The third layer has a thickness of 40 cm, and has relative dielectric constant ε of 35 and the conductivity σ of 0.003S/m. There is a water-filled no dense area with length, width and height of 15 cm in the third layer, and the center point of the no dense region is located in (0.2 m, 0.2 m, 0.48 m). In this paper, the porosity in this region is assumed to be 20%, the electric constants of two tenth of the nodal points in this region are defined as that of air, and these nodes are randomly distributed. The electric constants of the other nodes are the same as that of the third layer. All materials are assumed to be non-magnetic $\mu = 1$.

Transmitters and receivers are placed along the x- direction or the y- direction interface every 0.02 m for the reflection survey. The incident wave of 1GHz Ricker wavelet is still used in the simulation. The distance between the transmitter and receiver is 0.1 m. The incident source located at the transmitter in this model. The time interval and the space increment are chosen 0.001 ns and 0.005 m, respectively.

Table. 2 describes the parameters of the three-dimensional model. A schematic diagram of a three-dimensional model diagram can be displayed in Fig. 6. Fig. 7 gives the comparison of the dielectric constant section slices at x = 0.05 m, 0.25 m, 0.45 m, 0.65 m, 0.85 m, 1.05 m, 1.25 m, 1.45 m, 1.65 m, 1.85 m. Fig. 8 illustrates the comparison of the dielectric constant section slices at y = 0.05 m, 0.25 m,

TABLE 2. Description parameters of 3D Model.

Model name	Main parameters of the model (Unit: m)	Electrical parameters
Cracking	Extension (0~2) Width (0.01)	$\varepsilon = 1$, $\sigma = 0$
Square void	Length, width, height (0.1 , 0.1 , 0.1)	$\varepsilon = 1$, $\sigma = 0$
No dense region	Length, width, height (0.15 , 0.15 , 0.15)	$\varepsilon = 35 \sim 81$, $\sigma = 0.005S / m$

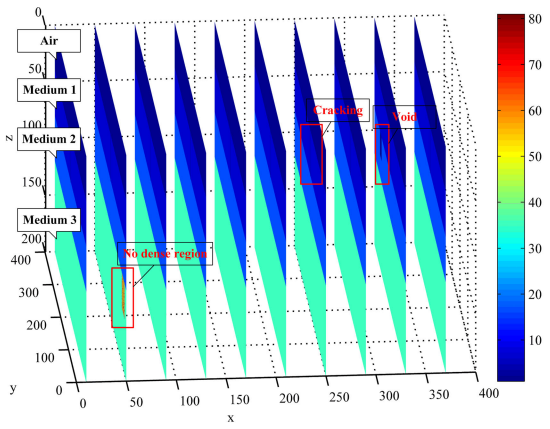

FIGURE 7. Comparison of the dielectric constant section slices at x = 0.05 m, 0.25 m, 0.45 m, 0.65 m, 0.85 m, 1.05 m, 1.25 m, 1.45 m, 1.65 m, 1.85 m.

0.45 m, 0.65 m, 0.85 m, 1.0 m, 1.25 m, 1.45 m, 1.65 m, 1.85 m.

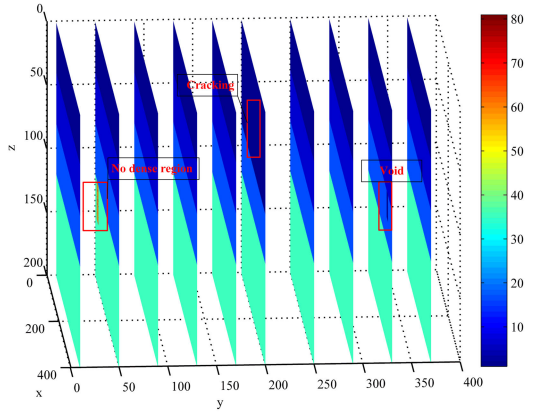

FIGURE 8. Comparison of the dielectric constant section slices at y = 0.05 m, 0.25 m, 0.45 m, 0.65 m, 0.85 m, 1.0 m, 1.25 m, 1.45 m, 1.65 m, 1.85 m.

It can be seen from Fig. 7 and Fig. 8, the dielectric constant distribution of the no dense region of the three-layer material can be seen in the slice at x = 0.25 m and y = 0.25 m, and the dielectric constant distribution of the material of the cracking can be clearly seen in the x-direction slice and in the slice at y = 1.0m. The dielectric constant distribution of the void can be seen on the slice at x = 1.65m and y = 1.65m. Due to the different dielectric constants of the materials set by different subsurface targets, the different slice plots of the two figures clearly demonstrate the distribution of the dielectric constant of the subsurface target material.

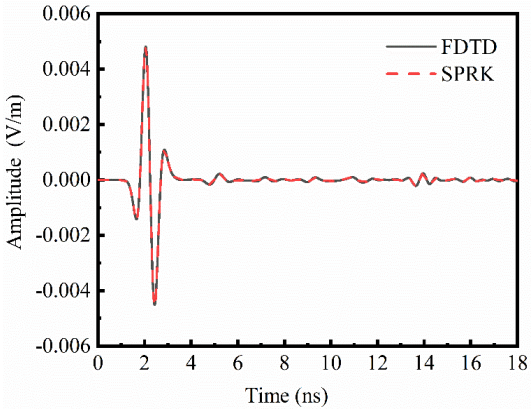

FIGURE 9. Comparison of the simulated results between SPRK method (red dash line) and the standard FDTD method (black solid line) at the point (1.0 m, 1.0 m, 0).

As shown in Fig. 9, the comparison of the simulated results between SPRK method and the standard FDTD method at the point (1.0 m, 1.0 m, 0). Fig. 10 displays the absolute errors at different time steps at the point (1.0 m, 1.0 m, 0 m). Fig. 11 illustrates the relative errors at different time steps at the point (1.0 m, 1.0 m, 0 m). As can be observed from these figures, excellent agreement is achieved. The error of the two algorithms mainly occurs where the amplitude fluctuates. This phenomenon is mainly caused by the difference in the differential iteration format of the two algorithms. The maximum absolute error does not exceed 0.00000015V/m and the maximum relative error is no more than 30%, and 95% of the relative errors are less than 15%. The proposed method achieves almost the same level of accuracy as the FDTD method.

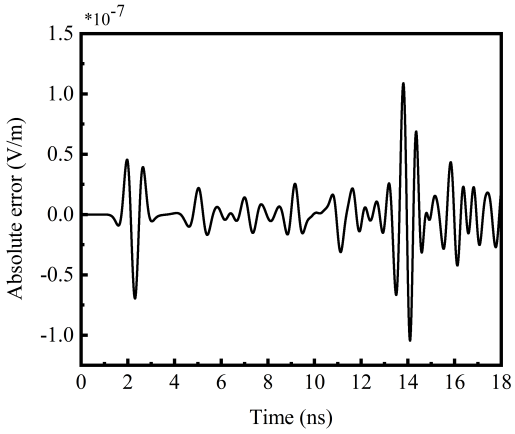

FIGURE 10. The absolute errors at different time steps at the point (1.0 m, 1.0 m, 0).

As shown in Fig. 12, the GPR reflected wave slices simulated at x = 0.05 m, 0.25 m, 0.45 m, 0.65 m, 0.85 m, 1.25 m,

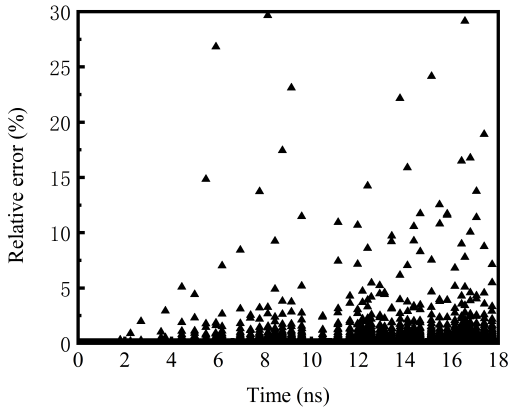

FIGURE 11. The relative errors at different time steps at the point (1.0 m, 1.0 m, 0).

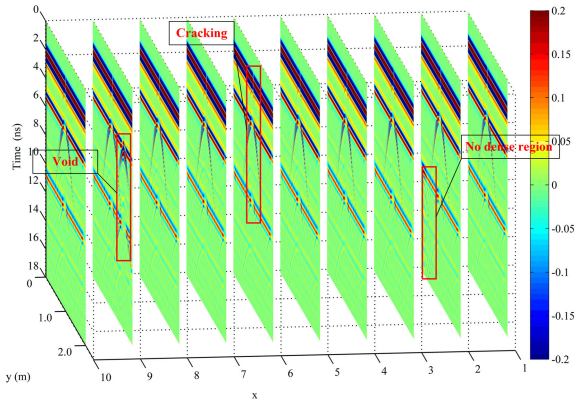

FIGURE 12. Comparison of the GPR slices at x = 0.05 m, 0.25 m, 0.45 m, 0.65 m, 0.85 m, 1.05 m, 1.25 m, 1.45 m, 1.65 m, 1.85 m.

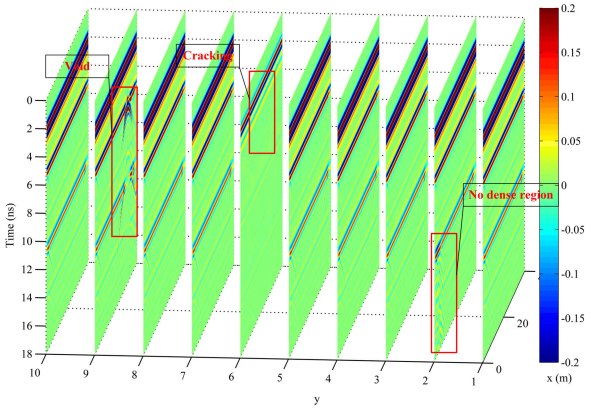

FIGURE 13. Comparison of the GPR slices at y = 0.05 m, 0.25 m, 0.45 m, 0.65 m, 0.85 m, 1.0 m, 1.25 m, 1.45 m, 1.65 m, 1.85 m.

1.45 m, 1.65 m, 1.85 m. Fig. 13 shows the GPR reflected wave slices at y = 1.85 m, 1.65 m, 1.45 m, 1.25 m, 1.0 m, 0.85 m, 0.65 m, 0.45 m, 0.25 m, 0.05 m. It can be seen from Fig. 12, the shape of the cracking is obviously shown in the slice at x-direction, the position of the no dense region can be obviously seen in the slice at x = 0.25 m, and the void can be obviously displayed in the slice at x = 1.65 m. The position of the water-filled no dense area in the slice at y = 0.25 m can be acquired in Fig. 13, and the position of the cracking of the first layer in the slice at y = 1 m can be acquired, and then the position of the void in the slice at y = 1.65 m can also be obtained.

Through the above figures, the accuracy of the proposed algorithm is basically the same as the traditional FDTD algorithm, however the 3D algorithm saves about 30% of the computational effort. The position of the underground targets can be accurately displayed by 3D numerical simulation.

VI. CONCLUSION

In this paper, we applied a relatively three-dimension SPRK method for GPR detection. Compared the traditional FDTD method with the SPRK method, the accuracy of the two method is basically the same. However, the SPRK method saves about 30% of the CPU time and increases memory consumption by less than 100 MB. The SPRK method can greatly improve the efficiency of forward simulation calculation of three-dimensional ground penetrating radar. Three-dimensional calculations can better reflect the distribution of media in space, and the accurate electromagnetic response information of the target can be obtained for GPR signals.

The proposed layered model is divided into rectangular meshes, which is simple and easy to operate. However, when the underground target is of curved or irregular shape, the step approximation is generated by using rectangular mesh subdivision, resulting in the generation of virtual wave in radar reflection in numerical simulation, which is disadvantageous for ground penetrating radar to accurately simulate underground targets. This is not conducive to the accurate simulation of underground targets by ground penetrating radar. Therefore, the next research work is how to accurately simulate three-dimensional underground targets.

REFERENCES

[1] Q. An, A. Hoorfar, W. Zhang, S. Li, and J. Wang, "Range coherence factor for down range sidelobes suppression in radar imaging through multilayered dielectric media," *IEEE Access*, vol. 7, pp. 66910–66918, 2019.

[2] J. M. Carcione, H. Marcak, G. Seriani, and G. Padoan, "GPR modeling study in a contaminated area of Krzywa Air base (Poland)," *Geophysics*, vol. 65, no. 2, pp. 521–525, 2000.

[3] A. Joshaghani, "Identifying the problematic areas with structural deficiencies of pavements using non-destructive tests (NDT)," *Int. J. Pavement Eng.*, vol. 20, no. 11, pp. 1359–1369, Nov. 2019.

[4] X.-K. Wei, W. Shao, and X.-H. Wang, "Hybrid sub-gridded time-domain method for ground penetrating radar simulations including dispersive materials," *IEEE Access*, vol. 6, pp. 15777–15786, 2018.

[5] W. C. Chew, F. L. Teixeira, M. Straka, M. L. Oristaglio, and T. Wang, "Parallel 3D PML-FDTD simulation of GPR on dispersive, inhomogeneous and conductive media," in *Proc. IEEE Antennas Propag. Soc. Int. Symp.*, Jul. 1997, pp. 380–383.

[6] T. M. Millington and N. J. Cassidy, "Optimising GPR modelling: A practical, multi-threaded approach to 3D FDTD numerical modelling," *Comput. Geosci.*, vol. 36, no. 9, pp. 1135–1144, 2010.

[7] I. Giannakis, A. Giannopoulos, and C. Warren, "Realistic FDTD GPR antenna models optimized using a novel linear/nonlinear full-waveform inversion," *IEEE Trans. Geosci. Remote Sens.*, vol. 57, no. 3, pp. 1768–1778, Mar. 2019.

[8] Y. Huang, J. Zhang, and Q. H. Liu, "Three-dimensional GPR ray tracing based on wavefront expansion with irregular cells," *IEEE Trans. Geosci. Remote Sens.*, vol. 49, no. 2, pp. 679–687, Feb. 2011.
[9] K. E. Schmidt and M. A. Lee, "Implementing the fast multipole method in three dimensions," *J. Stat. Phys.*, vol. 63, nos. 5–6, pp. 1223–1235, 1991.
[10] S. Negri, G. Leucci, and F. Mazzone, "High resolution 3D ERT to help GPR data interpretation for researching archaeological items in a geologically complex subsurface," *J. Appl. Geophys.*, vol. 65, nos. 3–4, pp. 111–120, 2008.
[11] Q.-W. Dai, H.-H. Wang, D.-S. Feng, and D.-P. Chen, "Finite element numerical simulation for GPR based on quadratic interpolation," *Progr. Geophys.*, vol. 27, no. 2, pp. 736–743, 2012.
[12] T. Namiki, "3-D ADI-FDTD method-unconditionally stable time-domain algorithm for solving full vector Maxwell's equations," *IEEE Trans. Microw. Theory Techn.*, vol. 48, no. 10, pp. 1743–1748, Oct. 2000.
[13] J. Li, Z. Zeng, L. Huang, and F. Liu, "GPR simulation based on complex frequency shifted recursive integration PML boundary of 3D high order FDTD," *Comput. Geosci.*, vol. 49, pp. 121–130, Dec. 2012.
[14] J. W. You and N. C. Panoiu, "Analysis of the interaction between classical and quantum plasmons via FDTD-TDDFT method," 2019, *arXiv:1904.06609*. [Online]. Available: https://arxiv.org/abs/1904.06609
[15] B. D. Welfert, "Analysis of iterated ADI-FDTD schemes for Maxwell curl equations," *J. Comput. Phys.*, vol. 222, no. 1, pp. 9–27, Mar. 2007.
[16] J. Yang, W. Cai, and X. Wu, "A high-order time domain discontinuous Galerkin method with orthogonal tetrahedral basis for electromagnetic simulations in 3-D heterogeneous conductive media," *Commun. Comput. Phys.*, vol. 21, no. 4, pp. 1065–1089, 2017.
[17] Y. Zhang, L. Wang, N. Feng, M. Zhuang, X. Feng, G. Fang, and Q. H. Liu, "A 3-D high-order reverse-time migration method for high-resolution subsurface imaging with a multistation ultra-wideband radar system," *IEEE J. Sel. Topics Appl. Earth Observ. Remote Sens.*, vol. 12, no. 2, pp. 744–751, Feb. 2019.
[18] I. Gladwell, G. Reddien, and J. Wang, "Energy superconvergence of one-step methods for separable Hamiltonian systems," *Phys. Lett. A*, vol. 209, nos. 1–2, pp. 31–38, 1995.
[19] W. Tang, Y. Sun, and J. Zhang, "High order symplectic integrators based on continuous-stage Runge-Kutta-Nyström methods," *Appl. Math. Comput.*, vol. 361, pp. 670–679, Nov. 2019.
[20] X. Kuang, Z. Huang, M. Chen, and X. Wu, "High-order symplectic compact finite-different time-domain algorithm for guide-wave structures," *IEEE Microw. Wireless Compon. Lett.*, vol. 29, no. 2, pp. 80–82, Feb. 2019.
[21] L. He and J. Li, "Symplectic critical surfaces with parallel normalized mean curvature vector in two-dimensional complex space forms," *Int. J. Math.*, vol. 30, no. 5, pp. 65–78, 2019.
[22] Z.-X. Huang and X.-L. Wu, "A second order symplectic partitioned Runge-Kutta scheme for Maxwell's equations," in *Proc. Asia–Pacific Microw. Conf.*, Dec. 2005, p. 4.
[23] H. Fang, G. Lin, and R. Zhang, "The first-order symplectic euler method for simulation of gpr wave propagation in pavement structure," *IEEE Trans. Geosci. Remote Sens.*, vol. 51, no. 1, pp. 93–98, Jan. 2013.
[24] M. Han, Q. Ma, and X. Ding, "High-order stochastic symplectic partitioned Runge-Kutta methods for stochastic Hamiltonian systems with additive noise," *Appl. Math. Comput.*, vol. 346, pp. 575–593, Apr. 2019.
[25] S. Liu, D. Yang, and J. Ma, "A modified symplectic PRK scheme for seismic wave modeling," *Comput. Geosci.*, vol. 99, pp. 28–36, Feb. 2017.
[26] R. L. Higdon, "Radiation boundary conditions for dispersive waves," *SIAM J. Numer. Anal.*, vol. 31, no. 1, pp. 64–100, 1994.
[27] R. L. Higdon, "Absorbing boundary conditions for elastic waves," *Geophysics*, vol. 56, no. 2, pp. 231–241, 1991.

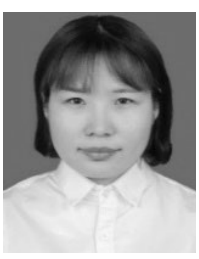

MAN YANG was born in Henan, China, in 1987. She received the B.S. and M.S. degrees in water conservancy and hydropower engineering from Zhengzhou University, Zhengzhou, China, in 2010 and 2013, respectively, where she is currently pursuing the Ph.D. degree in high-way and railway engineering.

Her research interests include nondestructive detection technique in engineering and numerical simulation methods including finite-difference time-domain method, finite-element method, and symplectic methods.

HONGYUAN FANG was born in Henan, China, in 1982. He received the B.S. and M.S. degrees in high-way and railway engineering from Zhengzhou University, Zhengzhou, China, in 2005 and 2008, respectively, and the Ph.D. degree in structural engineering from the Dalian University of Technology, Dalian, China, in 2012.

In 2012, he joined the Zhengzhou University, China, where he is currently a Professor with the School of Water Conservancy and Environment. His research interests include nondestructive detection technique in engineering and numerical simulation methods, includingfinite-difference time-domain method, finite-element method, and symplectic methods.

FUMING WANG was born in Henan, China, in 1957. He received the B.S. degree from the Zhengzhou Institute of Technology, Zhengzhou, China, in 1982, and the Ph.D. degree from the Dalian University of Technology, Dalian, China, in 1987.

In 1993, he joined the Zhengzhou University, China, where he is currently a Professor with the School of Water Conservancy and Environment. In 2015, he was elected as a member of the Chinese Academy of Engineering, Beijing, China. His research interests include nondestructive detection technique in engineering and numerical simulation methods in engineering, and computational electromagnetics, and the safety maintenance of infrastructure facilities.

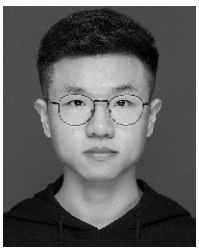

HEYANG JIA was born in Henan, China, in 1993. He received the B.S. degree in civil engineering from the North China University of Water Resources and Electric Power, Zhengzhou, China, in 2016, and the M.S. degree in traffic and transportation engineering from Zhengzhou University, Zhengzhou, in 2019, where he is currently pursuing the Ph.D. degree in safety and protection engineering.

JIANWEI LEI was born in Inner Mongolia, China, in 1993. He received the B.S. degree in road bridge and river-crossing engineering from the Zhengzhou University, Zhengzhou, China, in 2016, where he is currently pursuing the Ph.D. degree in safety and protection engineering. His research interests include nondestructive detection technique in engineering and numerical simulation methods, including finite-difference time-domain method, finite-element method, and sympletic methods.

DI ZHANG was born in Henan, China, in 1988. He received the degree in water conservancy and hydropower engineering from Hohai University, Nanjing, China, in 2012. He is currently with the Yellow River Conservancy Technical Institute. His research interests include UAV tilt photography and nondestructive testing in engineering.